Volume 53
Number 12
28 March 2024
Pages 5305-5734

Dalton Transactions

An international journal of inorganic chemistry

rsc.li/dalton

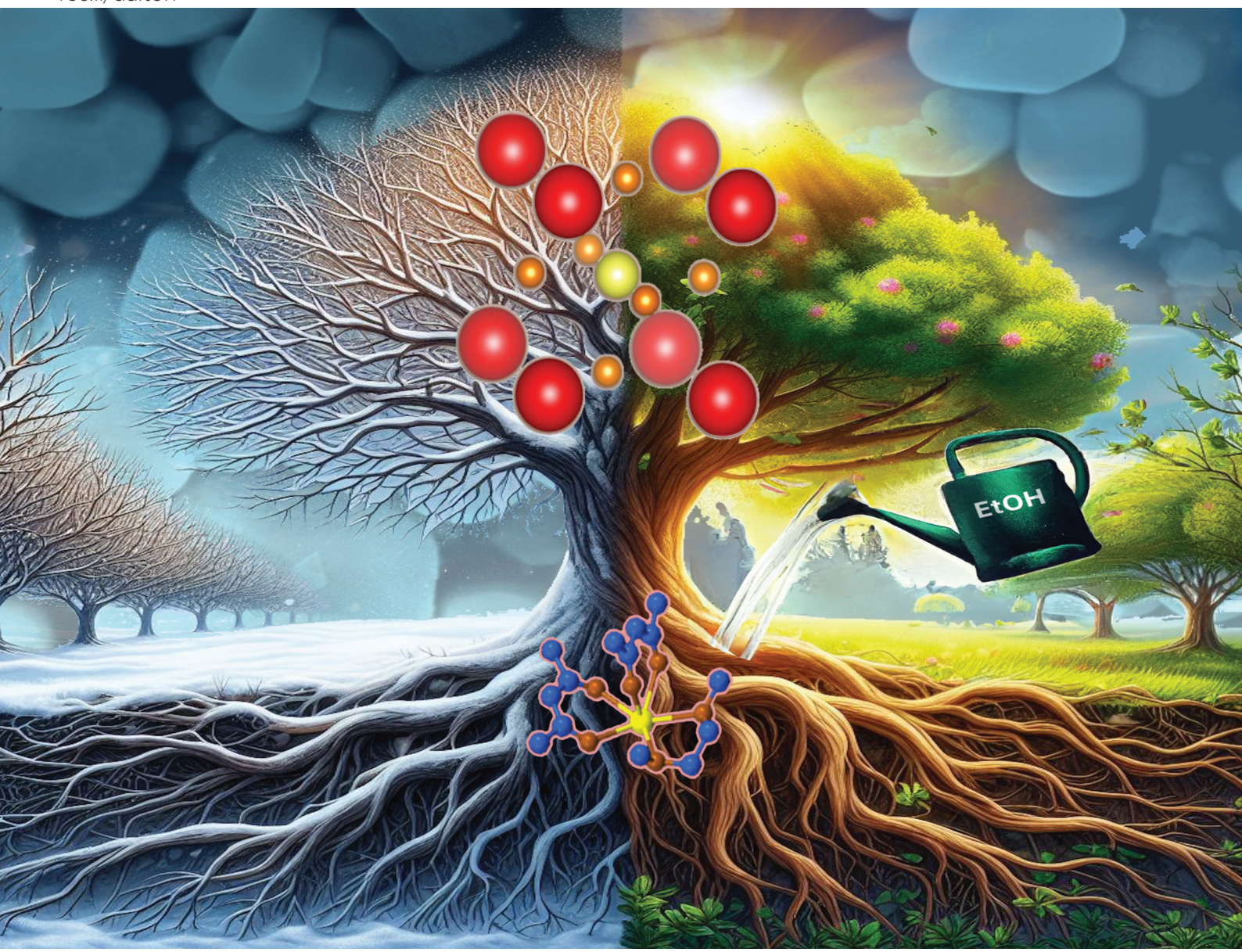

ISSN 1477-9226

ROYAL SOCIETY OF CHEMISTRY

PAPER

Anna Lucia Pellegrino, Graziella Malandrino *et al.*
Highly stable $CsPbBr_3$ perovskite phases from new lead β-diketonate glyme adducts

Dalton Transactions

ROYAL SOCIETY OF CHEMISTRY

PAPER

View Article Online
View Journal | View Issue

Cite this: *Dalton Trans.*, 2024, **53**, 5360

Highly stable $CsPbBr_3$ perovskite phases from new lead β-diketonate glyme adducts†

Lorenzo Sirna, [a] Anna Lucia Pellegrino,*[a] Salvatore Pio Sciacca,[a] Martina Lippi,[b] Patrizia Rossi, [b] Carmela Bonaccorso, [c] Giuseppe Bengasi,[d] Marina Foti[d] and Graziella Malandrino *[a]

Lead is one of the key metals of the all-inorganic lead halide perovskites. This work tailors novel architectures of lead's coordination sphere using a β-diketone (H-hfa = 1,1,1,5,5,5-hexafluoro-2,4-pentanedione) and a glyme (monoglyme, diglyme, triglyme, or tetraglyme) ligand. The coordination chemistry and thermal behaviour of these "$Pb(hfa)_2$·glyme" adducts have been analysed through FT-IR spectroscopy, ^1H and ^{13}C NMR analyses, thermogravimetric analysis (TGA), and differential scanning calorimetry (DSC). Single-crystal X-ray diffraction studies provide evidence of the formation of a monomeric $Pb(hfa)_2$·monoglyme structure. In order to validate the potentiality of these "$Pb(hfa)_2$·glyme" precursors for the fabrication of Pb-based halide perovskites, a facile, one-step and low-temperature solution approach has been applied to prepare $CsPbBr_3$ microcrystals with a process carried out in air under atmospheric pressure. Pure stoichiometric $CsPbBr_3$ powders, obtained using Cs(hfa) and Br_2 as cesium and bromide sources, respectively, show excellent stability under atmospheric conditions. Better results are obtained in terms of yield and stability from the diglyme and tetraglyme lead adducts. Field emission scanning electron microscopy (FE-SEM) indicates a good uniform morphology of cubic grains, while the structure and the 1 : 1 : 3 stoichiometry of Cs : Pb : Br are confirmed by X-ray diffraction (XRD) and energy dispersive X-ray analysis (EDX), respectively. Tauc plots derived from absorption spectroscopy point to optical energy band-gaps (E_g) in the 2.21–2.27 eV range, in agreement with literature data. The present research elucidates the potential of these novel "$Pb(hfa)_2$·glyme" adducts as promising lead precursors for $CsPbBr_3$ perovskite synthesis, paving the way for their implementation in various technological applications.

Received 29th November 2023,
Accepted 8th February 2024

DOI: 10.1039/d3dt03989g

rsc.li/dalton

1. Introduction

In the past few years, lead halide perovskites (LHPs), such as the hybrid organic–inorganic system of the type $CH_3NH_3PbX_3$ [1,2] (known as $MAPbX_3$, with MA = methylammonium cation) and $HC(NH_2)_2PbX_3$ [3] ($FAPbX_3$ in which FA is the formamidinium ion) or all-inorganic $CsPbX_3$ perovskites[4,5] (with X = Cl, Br, and I), have been intensively investigated.[6,7] In fact, they present unique properties such as a large light absorption coefficient,[8,9] fast generation of charge carriers,[10] a long carrier lifetime,[11] a high photoluminescence quantum yield (PLQY),[12,13] and a widely tunable band-gap.[14,15]

For these reasons, LHPs are suitable for a wide range of optoelectronic applications,[16,17] including light emitting diodes (LEDs),[18–20] photodetectors,[21,22] lasers,[23,24] and also catalysis[25,26] and solar cells.[27–29] Among them, the all-inorganic lead halide perovskites have attracted a lot of attention due to the as-mentioned optoelectronic properties and their improved stability.[30–33] This class of perovskites combines the benefits of having inexpensive and abundant elements with the stability of the structure because of the replacement of the organic component that is sensitive to the environment.[34,35] The all-inorganic lead halide perovskites present a structure of the general formula ABX_3 in which the A site is occupied by a Cs atom, the B site is occupied by an atom of Pb, and X is equal to Cl, Br, or I.[36]

Among them, the $CsPbBr_3$ phase represents an excellent candidate for a wide range of emerging technological applications. Particularly, $CsPbBr_3$ is investigated as an active material in photocatalysis[37] for fundamental organic reactions such as C–C, C–N, and C–O[38] bond formation and CO_2

[a]*Dipartimento Scienze Chimiche, Università degli Studi di Catania, and INSTM UdR Catania, Viale Andrea Doria 6, 95125 Catania, Italy.*
E-mail: annalucia.pellegrino@unict.it, graziella.malandrino@unict.it
[b]*Dipartimento di Ingegneria Industriale, Università di Firenze, Via Santa Marta 3, 50136 Firenze, Italy*
[c]*Dipartimento Scienze Chimiche, Università degli Studi di Catania, Viale Andrea Doria 6, 95125 Catania, Italy*
[d]*3SUN s.r.l., Contrada Blocco Torrazze, 95121 Catania, Italy*

†Electronic supplementary information (ESI) available: ^1H and ^{13}C NMR spectra; EDX spectra. CCDC 2304600 (**1**). For ESI and crystallographic data in CIF or other electronic format see DOI: **https://doi.org/10.1039/d3dt03989g**

reduction.[39] Furthermore, $CsPbBr_3$ crystals can be applied as a component for solar cells,[40] while nanocrystals have been used for the synthesis of a solid-state luminescent gas sensor.[41]

Typically, this kind of perovskite in the form of films or other structures (*i.e.* nanocrystals and quantum dots) is produced using solution processes.[42] However, most of these approaches are based on dissolving the precursors into organic solvents such as dimethyl sulfoxide (DMSO), *N*,*N*-dimethylformamide (DMF) and toluene[43] or require the use of surfactant species such as oleic acid (OA) and/or oleylamine (OLA).[44,45] For instance, Zhang and co-workers developed a solution-process for $MAPbX_3$ synthesis in which a perovskite solution was prepared by dissolving a 1 : 1 molar ratio of PbX_2 and MAX in DMF or DMF/DMSO (1 : 1).[46] Sun *et al.* reported the fabrication of a $CsPbBr_3$ film through the solubilisation of the CsBr and $PbBr_2$ precursors in DMSO.[47] On the other hand, vapor-phase methods were also intensively investigated.[48,49] A dual-source evaporation system was reported by Liu *et al.* to obtain a $CH_3NH_3PbI_{3-x}Cl_x$ perovskite[50] and by Huang *et al.* for the development of a $CsPbI_3$ based solar cell.[51] El Ajjouri and co-workers developed a single-source vacuum deposition in which CsX and PbX_2 were mixed in a crucible and then perovskite thin films were deposited in a high vacuum chamber.[52] However, although these methods are widely used, energetic conditions such as high temperatures or low pressures are required.

A lead ion presents a large ionic radius ($Pb(II)r_{6\text{-coord}}$ = 1.19 Å)[53] and for this reason it is responsible for interesting coordination moieties. In fact, different lead precursors are reported in the literature, such as tetraethyl ($PbEt_4$) and the lead triethyl alkoxide, $Et_3Pb(OR)$, where R is a *tert*-butyl or a neopentyl group.[54,55] However, these metalorganic compounds are extremely toxic due to their high volatility, *e.g.* the b.p. of $PbEt_4$ is around 80 °C and the temperature used for this precursor in the plasma enhanced chemical vapor deposition process of $PbTiO_3$ is −11 °C,[55] and this limits their possible wide applications.[56]

Among organic ligands, β-diketone is a mono-anion and is one of the most used ligand systems for the complexation of metal ions due to the two oxygen atoms in its structure, which offer a variety of metal–organic architectures as a bidentate ligand.[57–61] Lead β-diketonates are used as precursors in vapor phase processes, such as the case of $Pb(tmhd)_2$ [(H-tmhd = 2,2,6,6-tetramethyl-3,5-heptanedione)], $Pb(acac)_2$, [(H-acac = 2,4-pentanedione)], and their derivatives.[56,62]

It has been demonstrated that glymes, through oxygen-ion complexation, are very important for the stabilization of alkaline,[61,63,64] alkaline-earth[65,66] and rare-earth[67] metals. The presence of such a class of multidentate ligands, in fact, permits also to fine-tune the properties of the final metal adducts in terms of thermal stability, moisture- and air-sensitivity, solubility, and volatility. For instance, these compounds show good solubility in a large number of organic solvents.[57]

In this work we have developed novel lead precursors of the type "$Pb(hfa)_2$·glyme" [H-hfa = 1,1,1,5,5,5-hexafluoro-2,4-pentanedione, with glyme = monoglyme (1,2-dimethoxyethane), triglyme (2,5,8,11-tetraoxadodecane) and tetraglyme (2,5,8,11,14-pentaoxapentadecane)], by changing the polyether in order to investigate how the adducts' properties are affected by the glyme nature and in turn may influence the formation of the $CsPbBr_3$ phase. FT-IR spectroscopy, and ^1H and ^{13}C NMR analyses have been carried out to obtain information about the coordination of lead. Single-crystal X-ray diffraction of the $Pb(hfa)_2$·monoglyme has assessed the formation of a monomeric adduct. Thermogravimetric analyses (TGA), differential scanning calorimetry analyses (DSC), and melting point measurements have been used to investigate the thermal properties and stability of the adducts. In addition, for the sake of completeness, we also report the diglyme-based [(1-methoxy-2-(2-methoxyethoxy)ethane)] adduct, *i.e.* $[Pb(hfa)_2$·diglyme$]_2$, which had been previously reported and applied as a precursor in vapour-phase synthetic processes.[56]

Then, as a proof-of-concept of applications of these "$Pb(hfa)_2$·glyme" precursors, a facile, one-step and room-temperature solution approach has been applied to prepare $CsPbBr_3$ microcrystals. Cs(hfa) and Br_2 are used as cesium and bromide sources, respectively. The effects of the different ligands on the performance of lead adducts in $CsPbBr_3$ microcrystal formation are investigated. Structural, morphological, and compositional analyses of the final products, carried out through X-ray diffraction (XRD), field-emission scanning electron microscopy (FE-SEM), and energy dispersive X-ray analysis (EDX), respectively, are used to study the performance and the main characteristics of both the as-prepared and the six-month aged samples. Finally, the optical band gaps have been evaluated through Tauc plots starting from dispersions of $CsPbBr_3$ microcrystals.

2. Experimental

2.1 Materials and methods

Lead oxide (PbO), bromine (Br_2), and 1,1,1,5,5,5-hexafluoro-2,4-pentanedione (H-hfa, >98%), were purchased from Strem Chemicals and used without further purification. Monoglyme (1,2-dimethoxyethane, 99.5%), diglyme (bis(2-methoxyethyl) ether, 99.5%), triglyme (2,5,8,11-tetraoxadodecane, >98%), tetraglyme (2,5,8,11,14-pentaoxapentadecane, >99%), dichloromethane (CH_2Cl_2, >99.5%), ethanol (CH_3CH_2OH, 99.8%), and *n*-pentane ($CH_3(CH_2)_3CH_3$, ≥99%) were purchased from Sigma Aldrich.

2.2 General procedures

Synthesis of $Pb(hfa)_2$·monoglyme, 1. PbO (1.712 g, 7.7 mmol) 10% excess was suspended in dichloromethane (50 mL). Then, monoglyme (0.631 g per 0.727 mL, 7 mmol) was added to the suspension under stirring. Then, after 10 min, Hhfa (2.912 g per 2.000 mL, 14 mmol) was added, and the mixture was refluxed under stirring for 2 hours. The excess of PbO was filtered off. Light-yellow crystals were collected after the evaporation of dichloromethane. The reaction yield was 83%.

Synthesis of $[Pb(hfa)_2{\cdot}diglyme]_2$, 2. The precursor was synthesized using the procedure reported in ref. 56, from PbO (1.714 g, 7.7 mmol), 10% excess, suspended in dichloromethane (50 mL), diglyme (0.939 g per 0.996 mL, 7 mmol), and Hhfa (2.912 g per 2.00 mL, 14 mmol). Light-yellow crystals were collected after the evaporation of dichloromethane. The reaction yield was 89%.

Synthesis of $Pb(hfa)_2{\cdot}triglyme{\cdot}H_2O$, 3. The adduct was synthesized following the procedure described for **1**, from PbO (1.713 g, 7.7 mmol), 10% excess, triglyme (1.248 g per 1.267 mL, 7 mmol), and Hhfa (2.912 g per 2.000 mL, 14 mmol) in dichloromethane (50 mL). The resulting compound was sticky, so it was washed with ethanol. After the evaporation of the ethanol, light yellow sticky crystals were collected. The reaction yield was 71%.

Synthesis of $Pb(hfa)_2{\cdot}tetraglyme$, 4. The adduct was synthesized following the procedure for **1** from PbO (1.714 g, 7.7 mmol), about 10% excess, suspended in dichloromethane (50 mL), tetraglyme (1.556 g per 1.542 mL, 7 mmol) and Hhfa (2.912 g per 2.000 mL, 14 mmol). Light-yellow crystals were collected after the evaporation of dichloromethane. The reaction yield was 88%.

2.3 Precursor characterization

A Jasco FT/IR-430 spectrometer was used to record Fourier transform infrared (FT-IR) spectra with nujol mulls between NaCl plates.

NMR experiments in CD_3CN were carried out at 27 °C using a 500 MHz spectrometer (^{1}H NMR at 499.88 MHz and ^{13}C-NMR at 125.7 MHz) equipped with a pulse-field gradient module (*Z*-axis) and a tunable 5 mm Varian inverse detection probe (ID-PFG). Chemical shifts (δ) are reported in ppm and are referenced to a residual undertreated solvent.

A Kofler hot-stage microscope was used to measure the melting points of the precursors. Thermogravimetric analysis studies were performed using the STARe software and a Mettler Toledo TGA2. Dynamic thermal studies were carried out under purified nitrogen flow (50 sccm) under atmospheric pressure with a 5 °C min^{-1} heating rate. The weights of the samples were between 10 and 18 mg. Differential scanning calorimetry analyses were executed using a Mettler Toledo Star System DSC 3 calorimeter under purified nitrogen flow (30 sccm) and atmospheric pressure with a 5 °C min^{-1} heating rate. The weights of the samples were between 10 and 14 mg.

2.4 Single crystal X-ray structure

Single crystal X-ray diffraction data of $Pb(hfa)_2{\cdot}$monoglyme (**1**) were collected using a Bruker Apex-II diffractometer equipped with a CCD detector (T = 100 K; Mo-K$_\alpha$ radiation, λ = 0.71073 Å). For the data collection the APEX2 software was used,[68] while data integration and reduction were performed using the Bruker SAINT software.[69] The crystal structure was solved using the SIR-2004 package,[70] and refined by full-matrix least squares against F^2 using all data (SHELXL-2018/3).[71] Several crystals of $Pb(hfa)_2{\cdot}$monoglyme were tested and the data reported in the present article are those obtained for the best single crystal we were able to find. The chosen crystal was very small in order to avoid absorption problems. All the non-hydrogen atoms, with the exception of those belonging to disordered moieties (see below), were refined with anisotropic displacement parameters, while the hydrogen atoms were placed in a calculated position and their thermal parameter was set in accordance with that of the atoms to which they were bonded. All the fluorine atoms, with the exception of the three bonded to C5A (see Fig. S1†), were in disordered positions. Such disorder was modelled by using different models (three for the fluorine atoms bonded to C9B and two for all the other cases). In addition, the independent monoglyme molecule that coordinates Pb1A is affected by the disorder, that was modelled introducing two positions for all the carbon atoms (with the exception of C3, see Fig. S1†). All the disordered atoms were isotropically refined, while their occupancy factors were freely refined.

Geometrical calculations were performed by PARST97[72] and molecular plots were produced by the Mercury program (v4.1.2)[73] and Discovery Studio Visualizer 2019.[74] Crystallographic data and refinement parameters are reported in Table 1.

2.5 Synthesis of $CsPbBr_3$ microcrystals

The synthesis of the perovskite microcrystals took place through a precipitation reaction conducted by using the method illustrated in ref. 75, where $[Pb(hfa)_2{\cdot}diglyme]_2$ was used as lead source. The cesium precursor was synthesized through the procedure reported in ref. 76.

The precipitation reaction took place in an ethanol solution (EtOH 87 mmol, 5.024 ml) containing Cs(hfa) (1 mmol, 0.340 g) and "$Pb(hfa)_2{\cdot}$glyme" (1 mmol) through the addition of liquid Br_2 (1.5 mmol, 0.240 g). For the lead precursor, the following amounts were used for $Pb(hfa)_2{\cdot}$monoglyme (0.711 g), $[Pb(hfa)_2{\cdot}diglyme]_2$ (0.755 g), $Pb(hfa)_2{\cdot}triglyme{\cdot}H_2O$ (0.799 g) and $Pb(hfa)_2{\cdot}$tetraglyme (0.844 g). After precipitation, perovskite microcrystals were collected by filtration and dried

Table 1 Crystallographic data and refinement parameters for $Pb(hfa)_2{\cdot}$monoglyme

Empirical formula	$Pb(hfa)_2{\cdot}$monoglyme
Formula weight	711.425
Temperature (K)	100
Wavelength (Å)	0.71074
Crystal system, space group	Triclinic, $P\bar{1}$
Unit cell dimensions (Å, °)	a = 11.768(2); α = 76.220(4) b = 11.888(1); β = 74.385(4) c = 15.829(2); γ = 85.943(5)
Volume (Å^3)	2071.4(4)
Z, D_c (mg cm^{-3})	4, 2.281
μ (mm^{-1})	8.281
F(000)	668
θ range (°)	1.956–28.365
Reflections collected/unique	97 686/10 360
Data/parameters	10 360/593
Goodness-of-fit on F^2	1.017
Final R indices [$I > 2\sigma(I)$]	R_1 = 0.0409, wR_2 = 0.0812
R indices (all data)	R_1 = 0.0695, wR_2 = 0.0942

overnight in air. A yield in the range 50–60% was found for the $CsPbBr_3$ samples synthesized from $[Pb(hfa)_2{\cdot}diglyme]_2$, $Pb(hfa)_2{\cdot}triglyme{\cdot}H_2O$ and $Pb(hfa)_2{\cdot}tetraglyme$ precursors, while a yield of around 40% was obtained for the sample produced from the $Pb(hfa)_2{\cdot}monoglyme$.

2.6 Characterization of $CsPbBr_3$ microcrystals

Attenuated Total Reflection infrared spectra were recorded using a Spectrum Two FT-IR PerkinElmer spectrometer. XRD patterns were recorded in the Bragg–Brentano mode using a Smartlab Rigaku diffractometer equipped with a rotating Cu K_α anode operating at 45 kV and 200 mA. During the acquisition, a 0.02° increment step was used. A ZEISS Supra 55VP field-emission scanning electron microscope was used to carry out the morphological characterization using an electron beam energy of 15 keV. Samples of as-synthesized $CsPbBr_3$ microcrystals were attached to Al stubs using graphite double-sided adhesives in order to characterise the morphological features. The atomic composition of the powders was determined using energy dispersive X-ray (EDX) analysis by means of an INCA-Oxford "windowless" detector with a resolution of 127 eV, determined as the full width half maximum (FWHM) of the Mn K_α. The UV–vis spectra of the samples were collected utilizing an Agilent Cary 60 UV–vis spectrophotometer, using a dispersion of 2 mg of $CsPbBr_3$ microcrystals in 2 mL of ethanol.

3. Results and discussion

Novel lead complexes have been synthesized, in a single-step reaction, from the lead oxide, hexafluoroacetylacetone, and glyme ligands in dichloromethane. Each mixture has been refluxed under stirring for 2 hours through the following general equation:

$$PbO + 2Hhfa + glyme \rightarrow \text{“}Pb(hfa)_2 \cdot glyme\text{”} + H_2O$$

1 $Pb(hfa)_2{\cdot}monoglyme$
2 $[Pb(hfa)_2{\cdot}diglyme]_2$
3 $Pb(hfa)_2{\cdot}triglyme{\cdot}H_2O$
4 $Pb(hfa)_2{\cdot}tetraglyme$

After the solvent evaporation, precursors **1**, **2** and **4** were obtained as light-yellow crystals. Compound **3** had a yellow sticky crystal-like consistency.

3.1 Single crystal structure of $Pb(hfa)_2{\cdot}monoglyme$

Various attempts have been done to grow single crystals of **1**, **3** and **4**, but unfortunately only the single crystal of **1** was of good quality, with all the other single crystals twinned.

In the asymmetric unit of $Pb(hfa)_2{\cdot}monoglyme$, two independent Pb(II) complexes are present. In both units, the Pb(II) atom is hexa-coordinated, the donor atoms being the oxygen atoms of two hfa anions and those of a monoglyme molecule. In Fig. 1 an ORTEP view of the asymmetric unit of $Pb(hfa)_2{\cdot}monoglyme$ is reported.

The asymmetric disposition of the donor atoms around the metal cation may be related to the presence of the stereochemically active electron pair of Pb(II). As reported by Shimoni-Livay *et al.*,[77] while in high coordination number (9 and 10) Pb(II) complexes the disposition of the ligands around the metal cation is holodirected (*i.e.* the directional effect of the lone pair is less evident) and in low coordination number (2–5) complexes hemidirected geometries are usually found (for example showing Pb-donor bonds situated in a part of the sphere), in intermediate coordination number (6–8) lead complexes there can be active or inactive lone pairs. In the present case, both the fundamental geometrical features that indicated the presence of a stereochemically active electron pair (*i.e.* 1: a gap of coordination in the region where the lone pair was thought to be located and 2: a shortening of the distance between Pb and the donor atom located in the opposite side of a Pb(II) cation relative to the proposed site of the lone pair, in this case O1A and O1B) were observed.[56] The two independent $Pb(hfa)_2{\cdot}monoglyme$ complexes were quite well superimposa-

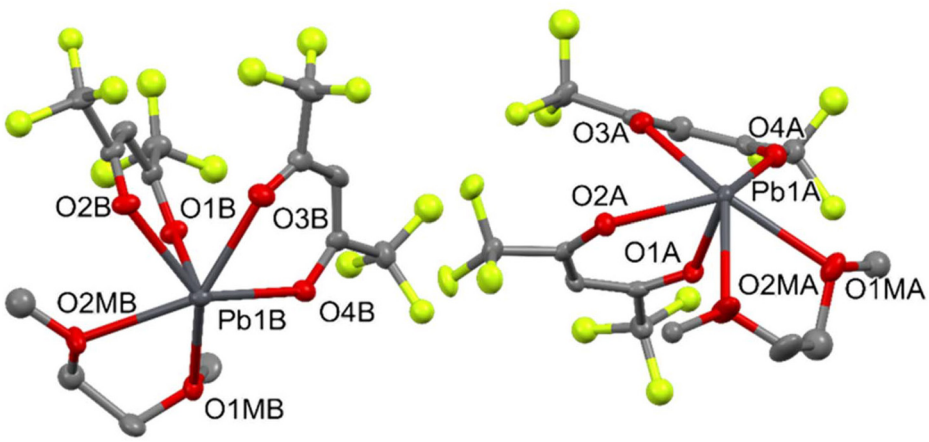

Fig. 1 Ortep-3 view of the asymmetric unit of $Pb(hfa)_2{\cdot}monoglyme$ (ellipsoid probability: 50%). Only the most populated models for the disordered moieties have been reported. For the sake of clarity hydrogen atoms have been omitted.

ble (see Fig. S2†) and the Pb-donor distances were in agreement with those observed in the Cambridge Structural Database (CSD)[78] for Pb/acac derivatives and Pb/ether complexes (see Table S1†).[79] Both the two independent complexes were involved in weak Pb···O interaction with a symmetry related complex (symmetry operation: $-x$, $-y$, $1-z$ and $1-x$, $1-y$, $-z$ for the Pb1A and Pb1B complexes, respectively) giving rise to the formation of dimers (see Fig. 2). Finally, no significant interactions between dimers were present in the crystal packing.

3.2 FT-IR characterization

All the "Pb(hfa)$_2$·glyme" precursors have been characterized by Fourier transform (FT)-IR spectroscopy in the 4000–400 cm^{-1} range. All the spectra have been recorded as nujol mulls.

As shown in Fig. 3a, the spectra of precursors **1**, **2** and **4** do not present any bands at 3600–3500 cm^{-1} related to the stretching of O–H. This aspect is indicative of the absence of water molecules coordinated to the metal ion for these adducts.

Adduct **3** presents, instead, a broad band at around 3500 cm^{-1} due to the presence of coordinated H_2O molecules.

Fig. 3b shows an enlargement of the FT-IR spectra of adducts **1**, **2**, **3** and **4** overlapped with the free H-hfa ligand spectrum. For the free ligand two peaks are observed at 1690 cm^{-1}, due to the C═O stretching, and at 1630 cm^{-1}, caused by the C═C stretching. For adducts **2**, **3** and **4** it can be observed that the peak related to C═O is slightly shifted at around 1675 cm^{-1}, while for adduct **1** it is possible to observe the peak at around 1650 cm^{-1}. This is indicative of hfa coordination to lead ion.

3.3 NMR characterization

The NMR spectra of "Pb(hfa)$_2$·glyme" complexes **1–4** have been recorded in CD_3CN; the complete signal attribution is reported in Table 2. The spectra clearly show the signal of both the polyether moieties and the hfa anions, as previously reported for similar complexes;[61,64] neither the ^{1}H nor the ^{13}C spectra show

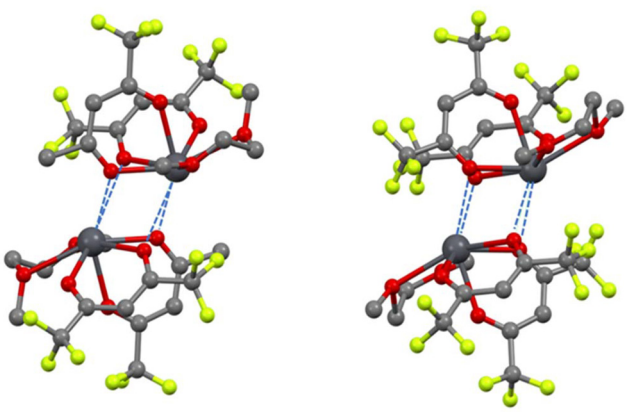

Fig. 2 Pb1A complex (left) and Pb1B complex (right) dimers in Pb(hfa)$_2$·monoglyme.

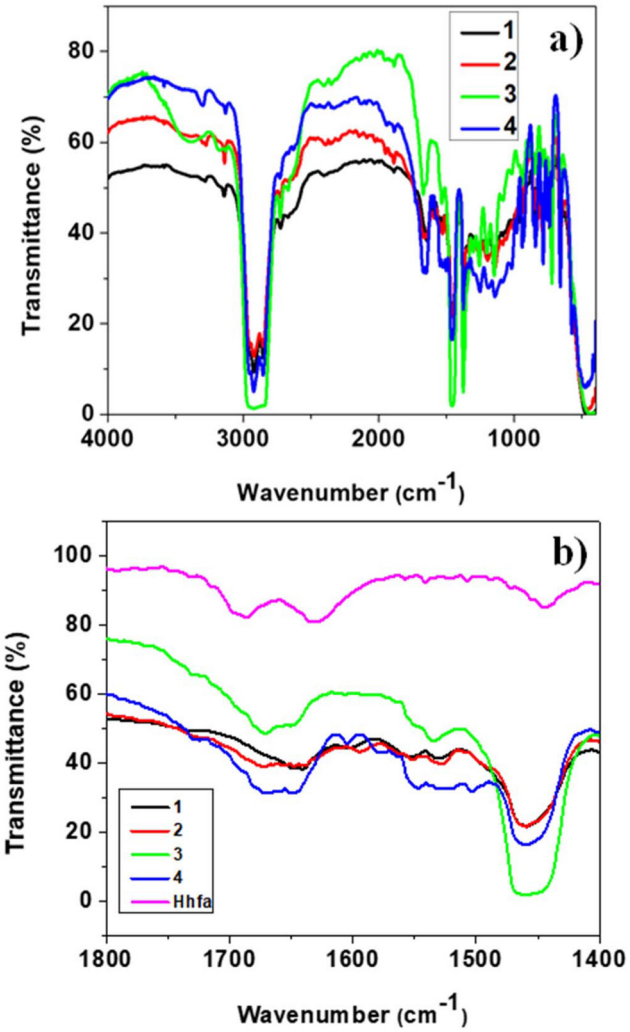

Fig. 3 (a) FT-IR spectra of **1**, **2**, **3** and **4** as nujol mulls in the 4000–400 cm^{-1} range. (b) Comparison of the FT-IR spectra of **1**, **2**, **3** and **4** with the free Hhfa ligand in the 1400–1800 cm^{-1} region.

evidence of tautomeric equilibria for the hfa moieties: the anionic enolate form is the only species observed in a solution for all the adducts.

In the ^{1}H-NMR spectra of the complexes (Table 2 and Fig. S3†), the polyether chains account for: (i) a singlet at 3.3–3.4 ppm, consistent with the terminal methyl groups, and (ii) the singlets/multiplets at slightly lower fields (3.5–3.7 ppm) for the inner methylenic protons. In all the complexes the proton of the hfa anion resonates as a singlet at lower fields, namely 5.8–5.9 ppm, and this is a clear indication of the deprotonation of the hfa ligand. Moreover, the integration values observed for adducts **1**, **2**, **3**, and **4** (reported in Table 2) confirm the expected stoichiometries and those defined by the X-ray diffraction analysis for **1** and **2**.

In the ^{13}C NMR spectra (Table 2, and Fig. S4†) we observe the signals of the hfa anions: the CH group resonates at 89–91 ppm, while the CF_3 and CO groups resonate as quartets (Fig. S5†), due to the coupling of ^{13}C with ^{19}F nuclei, at lower

Table 2 NMR data for the "Pb(hfa)glyme" complexes **1–4**

	^{1}H NMR		^{13}C NMR			
Complex	CO–C*H*=C–O$^-$	Polyether[a]	CO–*C*H=C–O$^-$	*C*O–CH=*C*–O$^-$	*C*F$_3$	Polyether[a]
1	5.90 (s, 2H)	a: 3.35 (s, 6H) b: 3.53 (4H)	90.63	175.23 (q, $^2J_{CF}$ = 33.7 Hz)	118.17 (q, $^1J_{CF}$ = 284.1 Hz)	a: 57.93 b: 71.41
2	5.88 (s, 2H)	a: 3.40 (s, 6H) b: 3.62 (m, 4H) c: 3.70 (m, 4 H)	90.05	175.04 (q, $^2J_{CF}$ = 33.2 Hz)	118.21 (q, $^1J_{CF}$ = 287.4 Hz)	a: 58.10 b: 69.78 c: 71.24
3	5.87 (s, 2H)	a: 3.40 (s, 6H) b: 3.63 (m, 4H) c, d: 3.74 (m, 8H)	89.67	174.88 (q, $^2J_{CF}$ = 32.9 Hz)	118.24 (q, $^1J_{CF}$ = 291.78 Hz)	a: 58.16 b: 69.36 c: 69.70 d: 71.02
4	5.81 (s, 2H)	a: 3.38 (s, 6H) b: 3.59 (m, 4H) c: 3.70 (m, 4H) d, e: 3.74 (m, 8H)	88.97	174.50 (q, $^2J_{CF}$ = 32.9 Hz)	118.29 (q, $^1J_{CF}$ = 288.5 Hz)	a: 57.95 b: 69.09 c: 69.24 d: 69.58 e: 70.91

[a] The notations used for the polyether moieties :are monoglyme (CH_3^a–O–CH_2^b)$_2$, diglyme (CH_3^a–O–$CH_2^bCH_2^c$)$_2$–O, triglyme (CH_3^a–O–CH_2^b–CH_2^c–O–CH_2^d–)$_2$, and tetraglyme (CH_3^a–O–CH_2^b–CH_2^c–O–CH_2^d–CH_2^e)$_2$–O.

fields ≈118 ppm and ≈175 ppm, respectively, with coupling constants of 284–290 Hz for $^1J_{CF}$ and 32–33 Hz for $^2J_{CF}$. The coordinated polyethers exhibit signals at 58 ppm for the terminal methyl groups, and at 69–71 ppm for the inner methylene carbons.

3.4 Thermal analysis

The thermal behaviour of the lead precursors has been investigated though thermogravimetric (TG) analysis (Fig. 4), differential scanning calorimetry (DSC) (Fig. 5), and the Kofler measurement of the melting points (values in the inset of Fig. 5).

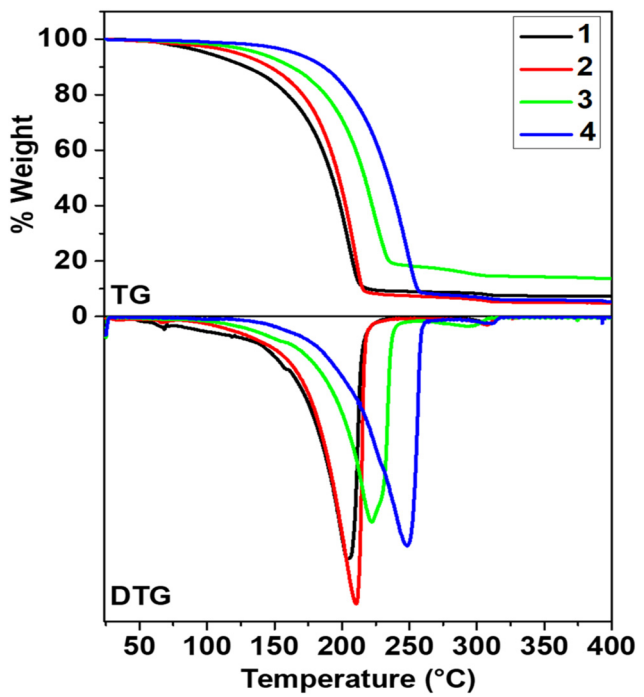

Fig. 4 TG and DTG profiles of **1**, **2**, **3** and **4** under N_2 flow and atmospheric pressure in the temperature range 25–400 °C.

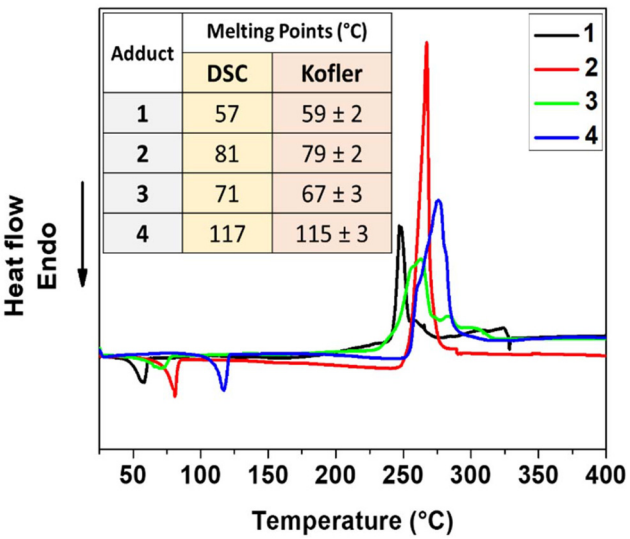

Fig. 5 DSC profiles of **1**, **2**, **3** and **4** under N_2 flow and atmospheric pressure in the temperature range 25–400 °C and melting points of the adducts through DSC curves and Kofler measurements.

TG curves (Fig. 4) of all the adducts show a single-step mass loss related to their vaporisation. In particular, at 350 °C, adducts **1**, **2** and **4** show a residue of about 7.4%, 5.1% and 5.9%, respectively. While at the same temperature, the TG curve of adduct **3** displays a higher residue of 14.3%.

Furthermore, for adduct **3**, we have carried out an energy dispersive X-ray analysis (EDX) of the residue of the TGA measurements in order to obtain information about the residue's nature and investigate the vaporization process. The spectrum, as shown in Fig. S6,† shows the presence of Pb and F peaks as main elements, while the presence of the carbon peak is likely related to the carbon tape used as support for the powder analysis.

Consequently, from the TG analyses it is evident that adducts **1**, **2**, and **4** present very low residues and a good thermal behaviour and thus these compounds are likely suitable not only in solution synthetic processes, taking advantage of their high solubility in common organic solvents, but also as precursors for vapor-phase methods.

To further investigate the thermal behaviour of the adducts, DSC characterization has been carried out and reported in Fig. 5. All the curves show endothermic peaks in the temperature range between 56 °C and 116 °C. These peaks may be related to the adduct melting processes. Notably, at higher temperature, in the range of 246–276 °C it is possible to observe for each complex the presence of exothermic peaks that can be likely associated with a partial decomposition overlapped with the incipient vaporization of the precursors.

Specifically, the DSC curves show endothermic peaks, associated with melting of the adducts, at 57 °C (**1**), 81 °C (**2**), 71 °C (**3**), and 117 °C (**4**).

All the information about the melting of the adducts obtained from the DSC curves are compared with the melting points obtained through a Kofler hot-stage microscope analyses, whose data are reported in the Fig. 5 inset table.

3.5 Synthesis, characterisation, and stability of $CsPbBr_3$ microcrystals

The four adducts have been applied for the synthesis of the $CsPbBr_3$ microcrystals through solubilization in ethanol together with the Cs(hfa) precursor and bromine. The samples are indicated as: **$CsPbBr_3$_1** for the sample obtained from Pb $(hfa)_2$·monoglyme, **$CsPbBr_3$_2** for the sample obtained from

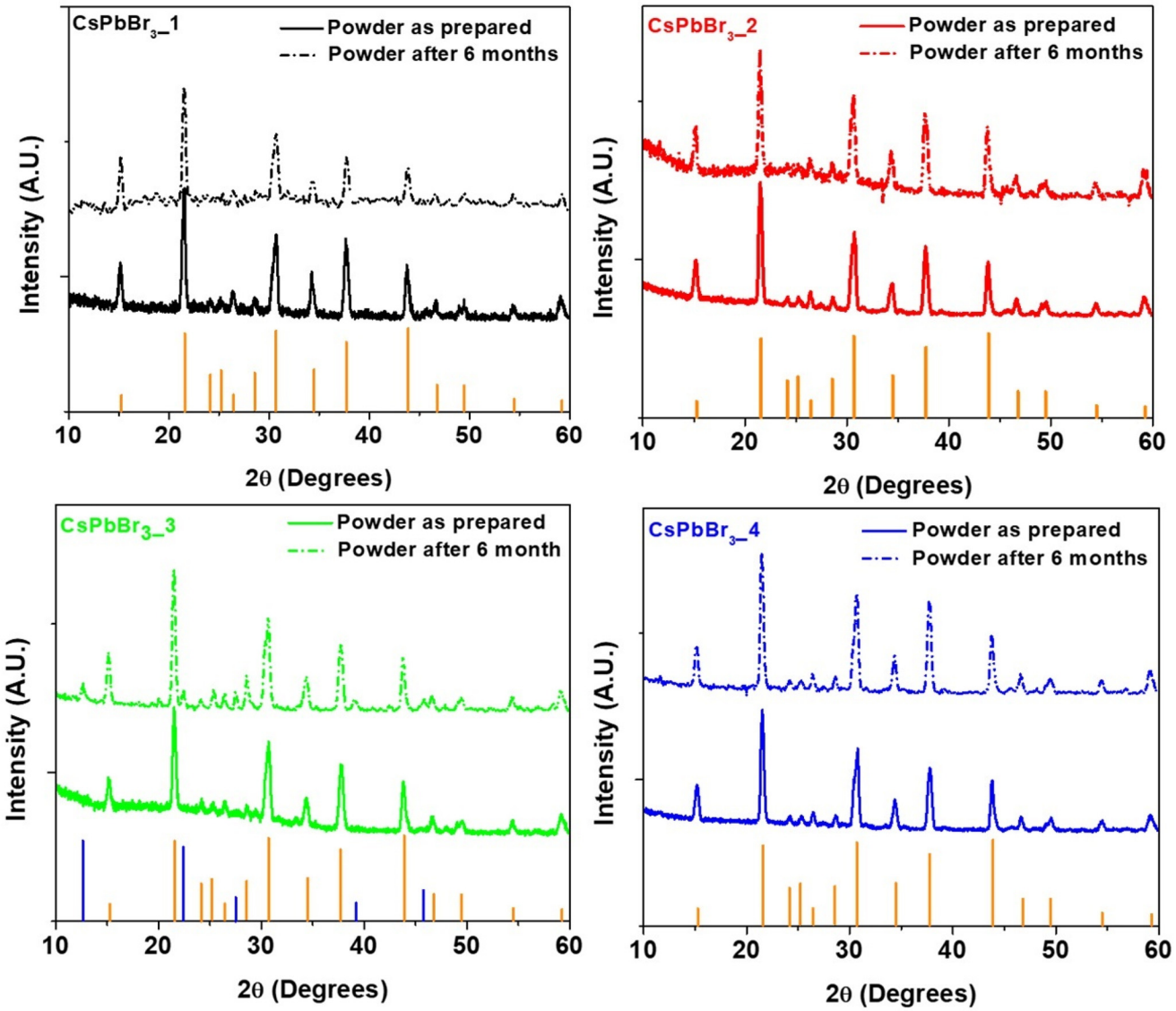

Fig. 6 XRD patterns of $CsPbBr_3$ microcrystals synthesized from Cs(hfa) and the "Pb$(hfa)_2$·glyme" precursor: (a) **$CsPbBr_3$_1**, (b) **$CsPbBr_3$_2**, (c) **$CsPbBr_3$_3**, and (d) **$CsPbBr_3$_4**. The continuous lines represent the as-prepared samples and the dotted lines represent the six-month aged samples. The orange lines represent the theoretical pattern of the $CsPbBr_3$ phase (ICDD n. 18-0364) and the blue ones are related to Cs_4PbBr_6 (ICDD n. 73-2478).

$[Pb(hfa)_2{\cdot}diglyme]_2$, **$CsPbBr_3$_3** for the sample obtained from $Pb(hfa)_2{\cdot}triglyme{\cdot}H_2O$, and **$CsPbBr_3$_4** for the sample obtained from $Pb(hfa)_2{\cdot}tetraglyme$. All the samples are seen by the naked eye as an intense orange colour. Some differences are observed in relation to the yield of the four samples; in particular the **$CsPbBr_3$_1** sample derived from the monoglyme adduct is produced in lower yield, about 40%, with respect to an average of 50–60% for the samples obtained from the other precursors.

The structural characterization of the as-prepared microcrystals **$CsPbBr_3$_1**, **$CsPbBr_3$_2**, **$CsPbBr_3$_3** and **$CsPbBr_3$_4** are shown in Fig. 6. The XRD patterns exhibit the formation of a pure $CsPbBr_3$ perovskite phase for all the four samples as confirmed by comparison with the diffraction file ICDD 18-0364. Therefore, all these precursors show good behaviour and suited reactivity in solutions to be applied to produce $CsPbBr_3$ through a simple precipitation method. Then, to investigate the stability of the as-prepared $CsPbBr_3$ samples, the microcrystals have been subjected to XRD characterization after 6 months of storage in air under atmospheric pressure.

Notably, the XRD patterns of the six-month aged $CsPbBr_3$ powders, obtained from adducts **1**, **2** and **4**, do not exhibit relevant changes with respect to the initial patterns, as shown in Fig. 6a, b and d, respectively, where the dotted line patterns represent the pattern of the aged samples. The peak positions and the intensities remain unchanged, suggesting the preservation of the perovskite structure and crystalline integrity. It is worth noting a different behaviour for the XRD pattern of **$CsPbBr_3$_3** after six-month storage (Fig. 6c, dotted line). In this case, we found traces of impurities associated with the Cs_4PbBr_6 phase,[80–82] as confirmed by comparison with the diffraction file ICDD 73-2478.

To obtain some hints on the different stability behavior of the four samples, FT-IR and TGA studies have been carried out on the four freshly synthesized $CsPbBr_3$ microcrystals in order to investigate the presence of ligands on the perovskite particle

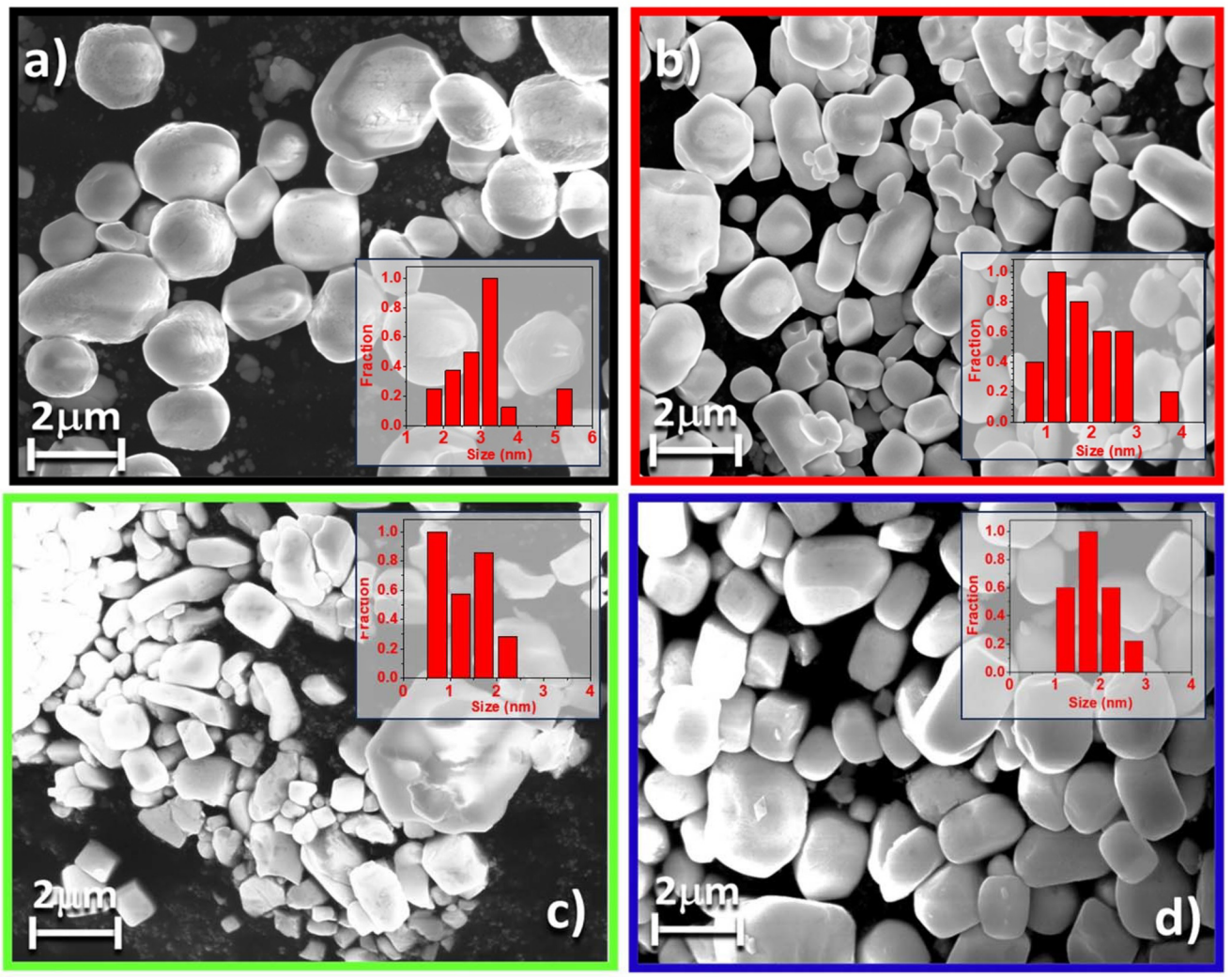

Fig. 7 FE-SEM images of $CsPbBr_3$ microcrystals synthesized from Cs(hfa) and the $Pb(hfa)_2{\cdot}glyme$ precursor: (a) **$CsPbBr_3$_1**, (b) **$CsPbBr_3$_2**, (c) **$CsPbBr_3$_3**, and (d) **$CsPbBr_3$_4**.

surface. The IR spectra of all the $CsPbBr_3$ samples have been recorded in the ATR mode to avoid any interference of the nujol or KBr matrix. Extremely small peaks are visible only in the *y*-axis enlarged graphic reported in the inset of Fig. S7.† As shown in the figure inset, the spectra of **$CsPbBr_3$_1**, **$CsPbBr_3$_2**, **$CsPbBr_3$_3** and **$CsPbBr_3$_4** have small peaks at around 1650, 1200 and 1100 cm^{-1}, associable with hfa ligand vibrational modes, thus indicating the possibility of a small amount of the hfa ligand coordinated to the perovskite samples. The **$CsPbBr_3$_3** sample also shows additional peaks at around 3450 and 2900 cm^{-1}. The peak at 3450 cm^{-1} is due to the O–H stretching mode, while the peak at 2900 cm^{-1} is likely due to the triglyme C–H stretching. The presence of these peaks indicates that very small traces of both ligands are present on the particle surface of the **$CsPbBr_3$_3** sample. TGA measurements confirm these hypotheses. In fact, a small weight loss in the range 5–7% is observed from 100 °C to 450 °C (Fig. S8†), which could be associated with the loss of adsorbed ligands. These findings may justify the different stability of the $CsPbBr_3$ samples derived from the four adducts, with the presence of a small amount of "H_2O" and triglyme likely affecting the instability after aging of the **$CsPbBr_3$_3** sample.

The morphological characterization of the as-prepared samples has been conducted through FE-SEM analysis and reported in Fig. 7. Fig. 7a, b and d, related to the microcrystals obtained from precursors **1**, **2** and **4**, respectively, show good uniformity in shape with mainly cubic grains. In particular, for the **$CsPbBr_3$_1** sample the grain dimensions are mainly picked at around 3 μm (inset in Fig. 7a). In the inset of Fig. 7b, the grains of the **$CsPbBr_3$_2** sample have a size of about 1–1.5 μm. Fig. 7c, instead, shows the FE-SEM image of the **$CsPbBr_3$_3** microcrystals. In this case the crystals are less regular in both dimensions and shape than those observed in

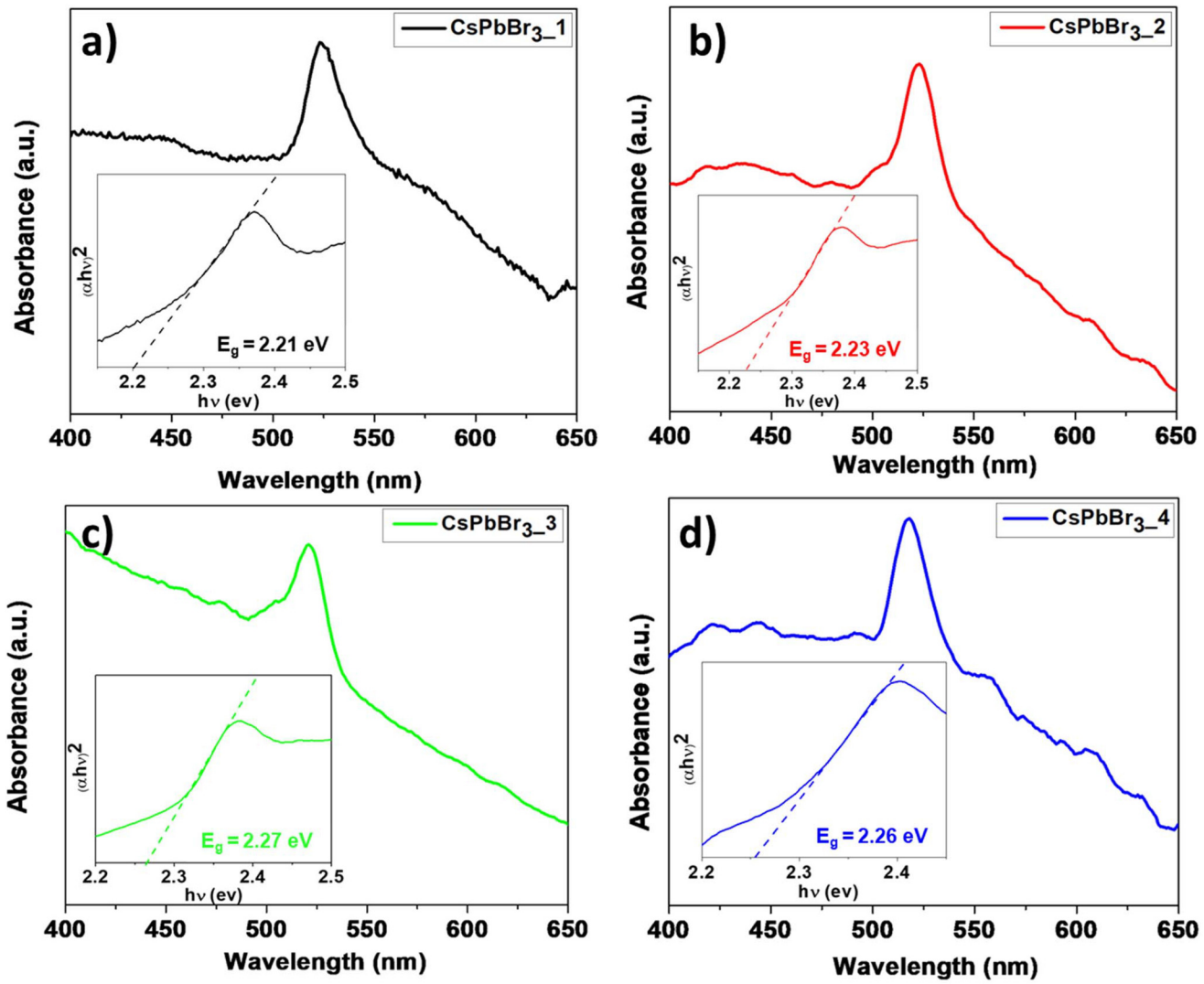

Fig. 8 UV–vis spectra of $CsPbBr_3$ microcrystals dispersed in ethanol synthesized from Cs(hfa) and the "$Pb(hfa)_2$·glyme" precursor: (a) **$CsPbBr_3$_1**, (b) **$CsPbBr_3$_2**, (c) **$CsPbBr_3$_3**, and (d) **$CsPbBr_3$_4**. In the inset, Tauc plot $(\alpha h\nu)^2$ against photon energy ($h\nu$) of the $CsPbBr_3$ powders. The dotted lines represent the linear extrapolation of the E_g value.

the other samples, and crystal size dimensions are in the range 1–2.5 μm (inset Fig. 7c). This trend can be likely rationalized considering the different reactivity of adduct **3** in the solution process may be due to the hydrated nature of the precursor, which leads to an inhomogeneity of the crystal precipitation process. Finally, a histogram of the sample **$CsPbBr_3$_4** (inset Fig. 7d) indicates an average dimension of the crystals of about 2 μm.

The composition of the $CsPbBr_3$ microcrystals has been determined through energy dispersive X-ray (EDX) analyses carried out on single grains. For each sample, several point-analyses have been collected in order to evaluate the homogeneity of the sample and confirm the correct stoichiometry of the $CsPbBr_3$ phase. For the microcrystals obtained from precursors **1**, **2**, **3** and **4**, the Cs : Pb : Br ratio is about 1 : 1 : 3, thus confirming the presence of the $CsPbBr_3$ perovskite phase (Fig. S9–S12†). Notably, in all the samples no peaks related to carbon (0.27 keV) or fluorine (0.67 keV), which could originate from the Cs(hfa) and "$Pb(hfa)_2$·glyme" precursors, are found. These results confirm a clean decomposition process of the precursors without any by-products, yielding the formation of bromide perovskite phases.

Finally, the precursors shown in this work may be applied to prepare $CsPbBr_3$ films. In fact, we recently reported for the $[Pb(hfa)_2$·diglyme$]_2$ precursor, that through the spray-coating of a solution containing the prepared microcrystals it is possible to deposit a thin film of $CsPbBr_3$.[83]

3.6 Optical properties of $CsPbBr_3$ microcrystals

To investigate the optical properties of the perovskite microcrystals, UV–vis analyses of the microcrystals dispersed in ethanol have been carried out. The absorbance spectra in the UV–vis range of the $CsPbBr_3$ powders obtained from the new Pb adducts have been used to derive the optical band-gap of the material. The optical band-gap energy (E_g) of the powders has been calculated from the absorption spectrum through the Tauc equation:[84]

$$(\alpha \cdot h\nu)^{\frac{1}{\gamma}} = B(h\nu - E_g)$$

where h is the Planck constant, ν is the frequency of the photon, E_g is the optical band gap energy, and B is a constant. The γ factor depends on the type of the electronic transition and is equal to $\frac{1}{2}$ or 2 for the direct and indirect transition band gaps, respectively.

The UV–vis spectra of the $CsPbBr_3$ dispersion in ethanol are reported in Fig. 8, while Tauc plots, obtained from the relation of $(\alpha h\nu)^2$ *versus* $(h\nu)$ calculated from the optical measurement, are reported as insets in the respective UV–vis spectrum graphs.

All the UV–vis spectra show a sharp absorbance ranging from 518 to 523 nm for the perovskite dispersion. Furthermore, the linear extrapolations from the Tauc's plots provide the following values for the direct optical band-gaps: 2.21 eV for **$CsPbBr_3$_1**, 2.23 eV for **$CsPbBr_3$_2**, 2.27 eV **$CsPbBr_3$_3** and 2.26 eV for **$CsPbBr_3$_4**.

The values of the absorption peak[17,81,85] and the optical band-gap values are in good agreement with literature data obtained under similar conditions.[86] Additionally, the E_g values are suitable for photon absorption in the visible region, making these microcrystals useful in a variety of optical applications.

4. Conclusions

In this study, novel lead complexes of the type "$Pb(hfa)_2$·glyme" were successfully synthesized using a single-step reaction involving lead oxide, hexafluoroacetylacetone and glyme ligands. Thermal analyses have demonstrated a good stability of these lead adducts, making them suitable for various applications, ranging from vapor to solution processes.

As a proof-of-concept, these lead complexes have been successfully applied as precursors, together with Cs(hfa) and Br_2, which were used as cesium and bromine sources, respectively, in a green solution synthesis of $CsPbBr_3$ microcrystals. The X-ray diffraction measurements confirmed the formation of the pure perovskite $CsPbBr_3$ structure from all the four Pb precursors. It is worth noting the excellent stability of the perovskite $CsPbBr_3$ microcrystals even after six months of storage under ambient conditions.

Among the four adducts, $Pb(hfa)_2$·monoglyme and $[Pb(hfa)_2$·triglyme·$H_2O]$ are the less promising adducts for the synthesis of the $CsPbBr_3$ microcrystals. In particular, $Pb(hfa)_2$·monoglyme produced the $CsPbBr_3$ microcrystals in a lower yield. On the other hand, $[Pb(hfa)_2$·triglyme·$H_2O]$ is less promising for different reasons: (i) a less homogeneous distribution of the **$CsPbBr_3$_3** crystal dimensions; and (ii) minor stability of the **$CsPbBr_3$_3** sample after six-month storage with respect to the other synthesized $CsPbBr_3$ samples. This finding may be related to the presence of H_2O in the coordination sphere, which is likely responsible for the presence of hydroxyl groups on the microcrystal surface. The good optical properties of this type of system are confirmed by UV–vis spectrophotometric analysis measurements, enabling a variety of applications, such as energy conversion and photocatalysis.

The present green solution synthesis shows numerous benefits including the absence of unsafe organic solvents and the mild working environment (room temperature and atmospheric pressure).

Finally, one of the biggest advantages of our approach is the possibility to deposit the perovskite film on highly thermally sensitive substrates such as PET or silicon solar cells. Our proof-of-concept paves the way for the use of our precursors for the preparation of flexible optoelectronic devices or silicon/perovskite tandem solar cells.

Author contributions

Lorenzo Sirna: investigation, formal analysis and writing – original draft. Anna Lucia Pellegrino: validation, data curation,

writing – review & editing. Salvatore Sciacca: investigation and data curation. Martina Lippi: investigation and data curation. Patrizia Rossi: methodology and validation. Carmela Bonaccorso: investigation and data curation. Giuseppe Bengasi: visualization and methodology. Marina Foti: visualization and methodology. Graziella Malandrino: supervision, funding acquisition and writing – review & editing.

Conflicts of interest

There are no conflicts to declare.

Acknowledgements

This research was funded by the University of Catania within the PIACERI research program UNICT 2020-22 Linea 2- project MatT-onE. A. L. P. and L. S. thank the Ministero dell'Università e della Ricerca within the PON "Ricerca e Innovazione" 2014-2020 Azioni IV.4 program. C. B. acknowledges the University of Catania for the funding received under the "PIAno di inCEntivi per la Ricerca di Ateneo 2020/2022 Pia.Ce.Ri. - Linea di intervento 3 Starting Grant - Project SiFiChrom. The authors thank Bionanotech Research and Innovation Tower (BRIT) laboratory of the University of Catania (Grant no. PONa3_00136 financed by the Italian Ministry for Education, University and Research, MIUR) for the diffractometer facility. Open access funding was provided by Università degli Studi di Catania.

References

1 A. Kojima, K. Teshima, Y. Shirai and T. Miyasaka, *J. Am. Chem. Soc.*, 2009, **131**, 6050–6051.
2 W. J. Nimens, J. Ogle, A. Caruso, M. Jonely, C. Simon, D. Smilgies, R. Noriega, M. Scarpulla and L. Whittaker-Brooks, *ACS Appl. Energy Mater.*, 2018, **1**, 602–615.
3 Y. Dou, S. Wang, C. Zhang, H. Luo, X. Li, H. Wang, F. Cao, P. Shen, J. Zhang and X. Yang, *Adv. Mater. Technol.*, 2020, **5**, 1901089.
4 E. Akman, T. Ozturk, W. Xiang, F. Sadegh, D. Prochowicz, M. M. Tavakoli, P. Yadav, M. Yilmaz and S. Akin, *Energy Environ. Sci.*, 2023, **16**, 372–403.
5 C. Wehrenfennig, G. E. Eperon, M. B. Johnston, H. J. Snaith and L. M. Herz, *Adv. Mater.*, 2014, **26**, 1584–1589.
6 H. Huang, M. I. Bodnarchuk, S. v. Kershaw, M. v. Kovalenko and A. L. Rogach, *ACS Energy Lett.*, 2017, **2**, 2071–2083.
7 A. K. Jena, A. Kulkarni and T. Miyasaka, *Chem. Rev.*, 2019, **119**, 3036–3103.
8 Y. Lei, Y. Chen, R. Zhang, Y. Li, Q. Yan, S. Lee, Y. Yu, H. Tsai, W. Choi, K. Wang, Y. Luo, Y. Gu, X. Zheng, C. Wang, C. Wang, H. Hu, Y. Li, B. Qi, M. Lin, Z. Zhang, S. A. Dayeh, M. Pharr, D. P. Fenning, Y. H. Lo, J. Luo, K. Yang, J. Yoo, W. Nie and S. Xu, *Nature*, 2020, **583**, 790–795.
9 J. P. Correa-Baena, A. Abate, M. Saliba, W. Tress, T. Jesper Jacobsson, M. Grätzel and A. Hagfeldt, *Energy Environ. Sci.*, 2017, **10**, 710–727.
10 X. Li, F. Cao, D. Yu, J. Chen, Z. Sun, Y. Shen, Y. Zhu, L. Wang, Y. Wei, Y. Wu and H. Zeng, *Small*, 2017, **13**, 1603996.
11 Z. Guo, Y. Wan, M. Yang, J. Snaider, K. Zhu and L. Huang, *Science*, 2017, **356**, 59–62.
12 L. Rao, Y. Tang, C. Song, K. Xu, E. T. Vickers, S. Bonabi Naghadeh, X. Ding, Z. Li and J. Z. Zhang, *Chem. Mater.*, 2019, **31**, 365–375.
13 Z. Li, C. Song, J. Li, G. Liang, L. Rao, S. Yu, X. Ding, Y. Tang, B. Yu, J. Ou, U. Lemmer and G. Gomard, *Adv. Mater. Technol.*, 2020, **5**, 1900941.
14 N. Pellet, J. Teuscher, J. Maier and M. Grätzel, *Chem. Mater.*, 2015, **27**, 2181–2188.
15 L. Rao, X. Ding, X. Du, G. Liang, Y. Tang, K. Tang and J. Z. Zhang, *Beilstein J. Nanotechnol.*, 2019, **10**, 666–676.
16 H. Dong, C. Ran, W. Gao, M. Li, Y. Xia and W. Huang, *eLight*, 2023, **3**, 1.
17 L. Protesescu, S. Yakunin, M. I. Bodnarchuk, F. Krieg, R. Caputo, C. H. Hendon, R. X. Yang, A. Walsh and M. v. Kovalenko, *Nano Lett.*, 2015, **15**, 3692–3696.
18 Y. Ren, J. Hua, Z. Han, M. Sun and S. Lü, *Chem. Eng. J.*, 2023, **452**, 139160.
19 Y. Tong, X. Bi, S. Xu, H. Min, L. Cheng, Z. Kuang, L. Yuan, F. Zhou, Y. Chu, L. Xu, L. Zhu, N. Zhao, N. Wang, W. Huang and J. Wang, *Adv. Mater.*, 2023, **35**, 2207111.
20 L. Rao, B. Sun, Y. Liu, G. Zhong, M. Wen, J. Zhang, T. Fu, S. Wang, F. Wang and X. Niu, *Nanomaterials*, 2023, **13**, 355.
21 X. Li, C. Liu, F. Ding, Z. Lu, P. Gao, Z. Huang, W. Dang, L. Zhang, X. Lin, S. Ding, B. Li, Y. Huangfu, X. Shen, B. Li, X. Zou, Y. Liu, L. Liao, Y. Wang and X. Duan, *Adv. Funct. Mater.*, 2023, 2213360.
22 W. Tian, H. Zhou and L. Li, *Small*, 2017, **13**, 1702107.
23 M. M. Stylianakis, T. Maksudov, A. Panagiotopoulos, G. Kakavelakis and K. Petridis, *Materials*, 2019, **12**, 859.
24 P. Liu, B. Yu, W. Cai, X. Yao, K. Chang, X. Zhao, Z. Si, W. Deng, Y. Zhou, G. Zhou and G. Wei, *J. Mater. Chem. C*, 2023, **11**, 2282.
25 Z. Y. Chen, N. Y. Huang and Q. Xu, *Coord. Chem. Rev.*, 2023, **481**, 215031.
26 S. Saris, A. Loiudice, M. Mensi and R. Buonsanti, *J. Phys. Chem. Lett.*, 2019, **10**, 7797–7780.
27 H. Zhang, M. K. Nazeeruddin and W. C. H. Choy, *Adv. Mater.*, 2019, **31**, 1805702.
28 N. N. Lal, Y. Dkhissi, W. Li, Q. Hou, Y. B. Cheng and U. Bach, *Adv. Energy Mater.*, 2017, **7**, 1602761.
29 X. Liu, J. Li, X. Cui, X. Wang and D. Yang, *J. Mater. Chem. C*, 2023, **11**, 426–455.
30 R. Montecucco, E. Quadrivi, R. Po and G. Grancini, *Adv. Energy Mater.*, 2021, **11**, 2100672.
31 C. Kang, S. Xu, H. Rao, Z. Pan and X. Zhong, *ACS Energy Lett.*, 2023, **8**, 909–916.
32 H. Mei, Y. Zhai, Q. Q. Zhu, N. Wu, H. Zhang, P. Liang and L. Wang, *Phys. Chem. Chem. Phys.*, 2023, **25**, 1279–1289.

33 C. Y. Huang, H. Li, Y. Wu, C. H. Lin, X. Guan, L. Hu, J. Kim, X. Zhu, H. Zeng and T. Wu, *Nano-Micro Lett.*, 2023, **15**, 16.
34 K. Huang, J. Liu, J. Yuan, W. Zhao, K. Zhao and Z. Zhou, *J. Mater. Chem. A*, 2023, **11**, 4487–4509.
35 S. Öz, A. K. Jena, A. Kulkarni, K. Mouri, T. Yokoyama, I. Takei, F. Ünlü, S. Mathur and T. Miyasaka, *ACS Energy Lett.*, 2020, **5**, 1292–1299.
36 Y. Zhao and K. Zhu, *Chem. Soc. Rev.*, 2016, **45**, 655–689.
37 S. Kumar, M. Regue, M. A. Isaacs, E. Freeman and S. Eslava, *ACS Appl. Energy Mater.*, 2020, **3**, 4509–4522.
38 X. Zhu, Y. Lin, J. San Martin, Y. Sun, D. Zhu and Y. Yan, *Nat. Commun.*, 2019, **10**, 2843.
39 Z. Chen, Y. Hu, J. Wang, Q. Shen, Y. Zhang, C. Ding, Y. Bai, G. Jiang, Z. Li and N. Gaponik, *Chem. Mater.*, 2020, **32**, 1517–1525.
40 J. Yu, G. Liu, C. Chen, Y. Li, M. Xu, T. Wang, G. Zhao and L. Zhang, *J. Mater. Chem. C*, 2020, **8**, 6326–6341.
41 E. Aznar-Gadea, I. Sanchez-Alarcon, A. Soosaimanickam, P. J. Rodriguez-Canto, F. Perez-Pla, J. P. Martínez-Pastor and R. Abargues, *J. Mater. Chem. C*, 2022, **10**, 1754–1766.
42 D. Zhang, S. W. Eaton, Y. Yu, L. Dou and P. Yang, *J. Am. Chem. Soc.*, 2015, **137**, 9230–9233.
43 S. Wei, Y. Yang, X. Kang, L. Wang, L. Huang and D. Pan, *Chem. Commun.*, 2016, **52**, 7265–7268.
44 X. Liang, R. W. Baker, K. Wu, W. Deng, D. Ferdani, P. S. Kubiak, F. Marken, L. Torrente-Murciano and P. J. Cameron, *React. Chem. Eng.*, 2018, **3**, 640–644.
45 D. Liu, C. Yang, M. Bates and R. R. Lunt, *iScience*, 2018, **6**, 272–279.
46 J. Zhang, C. Li, Y. Liang, J. Song, Q. Shang, L. Zhao, H. Tian, L. Liu and Q. Zhang, *Adv. Funct. Mater.*, 2023, **33**, 2208841.
47 K. Sun, Z. Bao, X. Guo, J. Ou, Y. Lv, D. Zou, L. Song, Y. Li, X. Liu and J. Liang, *J. Mater. Chem. C*, 2022, **10**, 9538–9545.
48 Q. Huang, Y. Liu, F. Li, M. Liu and Y. Zhou, *Mater. Today*, 2021, **47**, 156–169.
49 A. Ishteev, L. Luchnikov, D. S. Muratov, M. Voronova, A. Forde, T. Inerbaev, V. Vanyushin, D. Saranin, K. Yusupov, D. Kuznetsov and A. di Carlo, *Appl. Phys. Lett.*, 2021, **11**, 071901.
50 M. Liu, M. B. Johnston and H. J. Snaith, *Nature*, 2013, **501**, 395–398.
51 Q. Huang, F. Li, M. Wang, Y. Xiang, L. Ding and M. Liu, *Sci. Bull.*, 2021, **66**, 757–760.
52 Y. el Ajjouri, F. Palazon, M. Sessolo and H. J. Bolink, *Chem. Mater.*, 2018, **30**, 7423–7427.
53 R. D. Shannon, *Acta Crystallogr., Sect. A: Cryst. Phys., Diffr., Theor. Gen. Crystallogr.*, 1976, **32**, 751.
54 M. Shimizu and T. Shiosaki, *Mater. Res. Soc. Symp. Proc.*, 1995, **401**, 129.
55 M. Tong, G. Dai and D. Gao, *Mater. Lett.*, 2000, **46**, 60–64.
56 G. Malandrino, R. Lo Nigro, P. Rossi, P. Dapporto and I. L. Fragalà, *Inorg. Chim. Acta*, 2004, **357**, 3927–3933.
57 S. Mishra and S. Daniele, *Chem. Rev.*, 2015, **115**, 8379–8448.
58 A. Devi, *Coord. Chem. Rev.*, 2013, **257**, 3332–3384.
59 P. A. Vigato, V. Peruzzo and S. Tamburini, *Coord. Chem. Rev.*, 2009, **253**, 1099–1201.
60 R. C. Mehrotra, *Pure Appl. Chem.*, 1988, **60**, 1349–1365.
61 N. Peddagopu, A. L. Pellegrino, C. Bonaccorso, P. Rossi, P. Paoli and G. Malandrino, *Molecules*, 2022, **27**, 6282.
62 V. V. Krisyuk, I. A. Baidina and I. K. Igumenov, *Main Group Met. Chem.*, 1998, **21**, 4.
63 N. Peddagopu, S. Sanzaro, P. Rossi, P. Paoli and G. Malandrino, *Eur. J. Inorg. Chem.*, 2021, **36**, 3776–3780.
64 N. Peddagopu, P. Rossi, C. Bonaccorso, A. Bartasyte, P. Paoli and G. Malandrino, *Dalton Trans.*, 2020, **49**, 1002–1006.
65 M. E. Fragalà, R. G. Toro, P. Rossi, P. Dapporto and G. Malandrino, *Chem. Mater.*, 2009, **21**, 2062–2069.
66 F. lo Presti, A. L. Pellegrino and G. Malandrino, *Dalton Trans.*, 2022, **51**, 7352.
67 G. Malandrino and I. L. Fragalà, *Coord. Chem. Rev.*, 2006, **250**, 1605–1620.
68 Bruker, *Bruker APEX2*, Bruker AXS Inc., Madison, Wisconsin, USA, 2012.
69 Bruker, *Bruker SAINT*, Bruker AXS Inc., Madison, Wisconsin, USA, 2012.
70 M. C. Burla, R. Caliandro, M. Camalli, B. Carrozzini, G. L. Cascarano, L. De Caro, C. Giacovazzo, G. Polidori and R. Spagna, *J. Appl. Crystallogr.*, 2005, **38**, 381–388.
71 G. M. Sheldrick, *Acta Crystallogr., Sect. C: Struct. Chem.*, 2015, **71**, 3–8.
72 M. Nardelli, *J. Appl. Crystallogr.*, 1995, **28**, 659–659.
73 C. F. Macrae, I. J. Bruno, J. A. Chisholm, P. R. Edgington, P. McCabe, E. Pidcock, L. Rodriguez-Monge, R. Taylor, J. van de Streek and P. A. Wood, *J. Appl. Crystallogr.*, 2008, **41**, 466–470.
74 Dassault Systèmes BIOVIA, *Discovery Visualizer, v19.1.0.18287*, Dassault Systèmes, San Diego, 2019.
75 A. L. Pellegrino and G. Malandrino, *ACS Appl. Energy Mater.*, 2021, **4**, 9431–9439.
76 E. S. Vikulova, K. V. Zherikova, N. V. Kuratieva, N. B. Morozova and I. K. Igumenov, *J. Coord. Chem.*, 2013, **66**, 2235–2249.
77 L. Shimoni-Livny, J. P. Glusker and C. W. Bock, *Inorg. Chem.*, 1998, **37**, 1853–1867.
78 C. R. Groom, I. J. Bruno, M. P. Lightfoot and S. C. Ward, *Acta Crystallogr., Sect. B: Struct. Sci., Cryst. Eng. Mater.*, 2016, **72**, 171–179.
79 Pb–Oacac = compounds retrieved in the CSD: 41; fragments: 89, Pb–O distance range: 2.265–2.732 Å, mean value: 2.468 Å; Pb–Oether = compounds retrieved in the CSD: 117; fragments: 379, Pb–O distance range: 2.506–3.130 Å, mean value: 2.749 Å.
80 H. Lu, Y. Tang, L. Rao, Z. Li, X. Ding, C. Song and B. Yu, *Nanotechnology*, 2019, **30**, 295603.
81 G. C. Adhikari, S. Thapa, H. Zhu, A. Grigoriev and P. Zhu, *J. Phys. Chem. C*, 2019, **123**, 12023–12028.
82 Z. Bao, H. C. Wang, Z. F. Jiang, R. J. Chung and R. S. Liu, *Inorg. Chem.*, 2018, **57**, 13071–13074.

83 L. Sirna, A. L. Pellegrino, F. Lo Presti, F. Faini, G. Grancini, G. Bengasi, M. Foti and G. Malandrino, *Appl. Surf. Sci.*, 2023, **622**, 156916.
84 P. Makuła, M. Pacia and W. Macyk, *J. Phys. Chem. Lett.*, 2018, **9**, 6814–6817.
85 L. Protesescu, S. Yakunin, O. Nazarenko, D. N. Dirin and M. V. Kovalenko, *ACS Appl. Nano Mater.*, 2018, **1**, 1300–1308.
86 A. Bhardwaj and A. K. Kushwaha, *ECS J. Solid State Sci. Technol.*, 2022, **11**, 036002.